Electrokinetic flow of fluids with pressure-dependent viscosity and slip-dependent zeta potential

Jiachen Yuan(袁嘉晨),Yuran Qiao(乔煜然), Jifeng Cui(崔继峰) and Xingyu Chen(陈星宇)*

College of Science, Inner Mongolia University of Technology, Hohhot, Inner Mongolia 010051, China

* Author to whom correspondence should be addressed: xychen@imut.edu.cn

ABSTRACT

This paper investigates the electrokinetic flow and electrokinetic energy conversion efficiency(EKEC) of fluids characterized by pressure-dependent (P.D.) viscosity and slip-dependent (S.D.) zeta potential within a slip channel. Using the exponential pressure-viscosity relationship, we derive the electrokinetic flow characteristics of the fluid by solving the continuity and two-dimensional momentum equations with the perturbation method. A systematic study is then conducted on the influence of S.D. zeta potential and the effect of P.D. viscosity on the pressure, viscosity, velocity, streaming potential, and electrokinetic energy conversion efficiency. The results show that the P.D. viscosity effect increases the pressure and the fluid viscosity, but reduces the electrokinetic energy conversion efficiency. The S.D. zeta potential effect enhances the pressure, fluid viscosity, axial velocity, vertical velocity, and streaming potential, and markedly improves the EKEC. The results reveal that Case II (pressure-independent viscosity and slip-dependent zeta potential) achieves a higher energy conversion efficiency than the other three cases. In the pressure-dependent viscosity cases, the slip-dependent zeta potential effect improves the maximum conversion efficiency from 7.5% to 10.9%, an improvement of 45.33%. This study provides a theoretical reference for modeling the fluid flow involving pressure-dependent viscosity and slip-dependent zeta potential.

Keywords: Electrokinetic flow; Slip-dependent zeta potential; Pressure-dependent viscosity; Electrokinetic energy conversion

PACS:47.11.Bc, 47.65.–d, 47.85.Dh

1. Introduction

In recent years, the flow behavior and transport mechanisms in micro/nano-scale devices have attracted increasing attention from the academic community.[1-5] Accordingly, significant progress has been made in micro/nanofluidic transport technologies in cutting-edge fields such as renewable energy, microelectromechanical systems (MEMS), biochips, portable electronic devices, and energy harvesting.[6-10] Central to these technologies is microfluidic technology, which focuses primarily on the driving and manipulation of fluids within micro/nanochannels. Fluid flow is typically achieved using mechanisms such as pressure, electric fields, and magnetic fields.[11,12] Among these

mechanisms, pressure-driven schemes offers advantages including compact structure, low energy consumption and high mobility.[13]

When an electrolyte solution flows through micro/nanochannels, spontaneous chemical reactions at the solid-liquid interface cause the formation of an electrical double layer (EDL).[14-19] When a pressure gradient is imposed along the axis, the excess charges within the EDL are advected toward the downstream end, generating a streaming current.[20,21] The accumulation of net charges at the downstream end induces a streaming potential field opposite to the flow direction. Concurrently, the streaming potential generates an opposing ionic current, known as the conduction current. Under steady-state conditions, the streaming current and conduction current balance each other, resulting in a net current of zero.[22-24] Consequently, the opposing streaming potential field resists fluid flow, leading to a reduction in flow velocity, which is referred to as the electroviscous effect.[25-28] By channeling the streaming current through an external circuit, electrical energy can be harvested from the mechanical energy of the flowing fluid.[29-31] This energy conversion mechanism based on electrokinetic phenomena is called electrokinetic energy conversion.[32-34]

Over the last several decades, substantial research endeavors have been devoted to improving EKEC efficiency through various optimization strategies, including modifying geometric shapes, using non-Newtonian fluids, and considering steric and slip effects.[35-40] For example, previous studies demonstrated that interfacial slip can significantly enhance EKEC efficiency.[41-43] Such studies treat the zeta potential as independent of interfacial slip. The wall slip velocity is subsequently evaluated through the Navier slip condition, in which the slip length is taken as constant. However, in microfluidic electrokinetic flows the channel walls are charged, and interfacial slip affects both the surface charge and the apparent zeta potential. Jing and Bhushan [44] provided a thorough review of the interplay between surface charge and interfacial slip. Based on measurements on KCl solutions in methylated quartz capillaries, Churaev et al. [45] proposed a linear relationship between the zeta potential and interfacial slip. Subsequently, based on the analytical solution for oscillatory flow in parallel plates, Yang and Kwok [46] found that slip can alter the zeta potential and reduce the velocity gradient within the Debye layer, thereby influencing electrokinetic behavior. Similarly, Tretheway and Meinhart[47] reported that a slip-dependent zeta potential can significantly increase the fluid velocity in hydrophobic microchannels. Later, Tandon and Kirby[48] proposed a nonlinear model for symmetric electrolytes, which accurately describes the effect of slip length at high zeta potentials. Recently, Liu et al.[49] proposed an ion transport model coupling surface charge and boundary slip effects, revealing a strong interdependence between surface charge and slip length. Their findings revealed that boundary slip plays a beneficial role in electrokinetic performance. In particular, it can markedly boost the output power and energy conversion efficiency,

with maximum values reaching 2.7 pW and 30%, respectively.

In the aforementioned studies, fluid viscosity is assumed constant. However, in high-pressure driven flows, such as the manufacturing of composite prepregs, processing of polymer macromolecules and elastohydrodynamic lubrication, fluid viscosity can change significantly with pressure.[50,51] Consequently, it is necessary to investigate flows of fluids with pressure-dependent viscosity. For instance, Hron et al. [52] proposed a linear pressure-dependent viscosity model to study problems such as unidirectional flow and plane parallel flow. Rajagopal et al.[53] analyzed the non-steady flow of pressure-dependent viscous fluids under gravitational effects, analyzing qualitative aspects such as the existence and uniqueness of solutions to the governing equations. For steady, isothermal, pressure-driven flows in straight channels and circular tubes, Housiadas[54,55] derived exact or approximate solutions for viscoelastic fluids with pressure-dependent viscosity, providing a theoretical modeling basis. Recently, Herbst et al. [56] studied the flow of incompressible power-law fluids exhibiting pressure-dependent viscosity in convergent channels. In micro/nanochannels, the pressure-dependent viscosity effect likewise cannot be neglected. For example, Cui et al.[57] measured the flow of liquids in microtubes over driving pressures of 1-30 MPa and observed that isopropanol and carbon tetrachloride deviate from the classical Hagen-Poiseuille prediction at high pressure. By examining tube deformation, liquid compressibility, viscous heating and wall slip, they concluded that the pressure-dependent viscosity is largely responsible for these discrepancies. Silber et al. [58] adopted the Hagen-Poiseuille equation with slip boundary conditions together with Bridgman's pressure-viscosity exponential relation to resolve the nonlinear axial pressure variation inside microtubes. The modified Poiseuille number incorporating the pressure-dependent viscosity achieves satisfactory consistency with high-pressure experimental measurements of isopropanol. Their results verify that the pressure dependence of viscosity change serves as a predominant factor for liquid flows under large driving pressures.

In this work, we systematically investigate electrokinetic flow and energy conversion of fluids considering the effects of pressure-dependent viscosity and slip-dependent zeta potential. Going beyond the conventional unidirectional-flow assumption, we obtain the distributions of velocity, pressure, and viscosity by solving the two-dimensional governing equations. Four distinct cases are further established (Case I: pressure-independent (P.ID.) viscosity and slip-independent (S.I.) zeta potential; Case II: P.ID. and S.D.; Case III: P.D. and S.I.; Case IV: P.D. and S.D.) to analyze the effects of slip-dependent zeta potential and pressure-dependent viscosity on the pressure, velocity, electroviscous effect, input power, output power, and EKEC efficiency. The analytical solutions obtained here can also act as a reference for validating numerical simulations of more complex models.

2.Model description

A theoretical investigation of the pressure-driven electrokinetic flow in a parallel-plate channel is presented, accounting for both pressure-dependent viscosity and slip-dependent zeta potential, as illustrated in Fig. 1. A Cartesian coordinate system (x^*,y^*) is established at the channel entrance. The channel height is $2H^*$, the width is W^* and the length is L^*. The length is assumed to be much larger than the height and the width, i.e., $L^*>>2H^*$ and $L^*>>W^*$. The channel is filled with an incompressible electrolyte solution, and an electrical double layer (EDL) forms at the interface between the solution and the charged channel wall. The effective zeta potential is $\psi_\gamma{}^*$, which depends on the slip length.[32,45] When a high pressure difference is applied across the two ends of the channel along the x^*-direction, the pressure is non-uniform in the channel, thereby causing the local viscosity to vary, denoted by $\eta^* = \eta^*(p^*)$.[55] At the same time, net charge within the EDL is advected downstream, and the resulting surplus of charge creates a higher electrical potential downstream than upstream, generating a reverse electric field, known as the streaming potential $E_s{}^*$.[30,49]

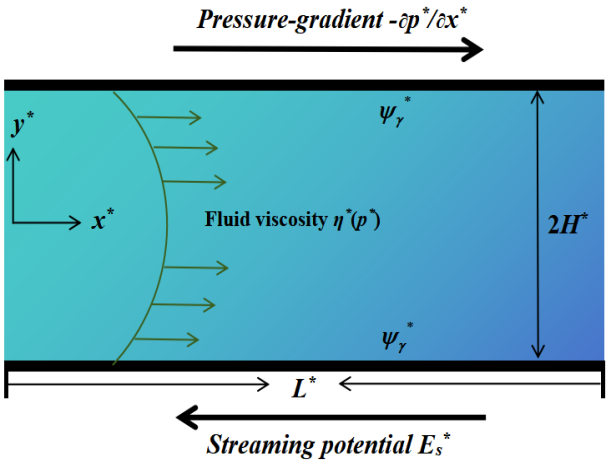


Fig. 1. Schematic diagram of pressure-driven electrokinetic flow of fluids with pressure-dependent viscosity in a parallel-plate channel.

2.1. Electrical potential distribution

As the electrolyte solution flows through the channel, the channel surface acquires charge through chemical reactions, spontaneously giving rise to an EDL at the solid-liquid interface. According to EDL theory, provided that the channel length far exceeds its height and width, the electricl potential ψ^* is governed by a one-dimensional Poisson equation:[18,25,26]

$$\frac{d^2\psi^*}{dy^{*2}} = -\frac{\rho_e^*}{\varepsilon_0\varepsilon_r}, \tag{1}$$

where ε_0 is the vacuum permittivity and ε_r is the relative permittivity. For a symmetric electrolyte solution,[18,25,26] and neglecting ionic volume and variations in the dielectric constant, the ions follow the Boltzmann distribution.[18,25,26] The net charge density $\rho_e{}^*$ in the electrolyte solution is given by:

$$\rho_e^* = -2n_\infty e_0 z_v \sinh(\frac{e_0 z_v \psi^*}{k_B T}), \tag{2}$$

where e_0 is the elementary charge, n_∞ is the bulk ionic number concentration of ions in the electrolyte solution, z_v is the ion valence, k_B is the Boltzmann constant, and T is the absolute temperature. If the electrical potential ψ^* remains well below 25 mV, the electrostatic energy is significantly lower than the thermal energy, i.e., $|e_0 z_v \psi^*/k_B T| << 1$. Accordingly, Eq. (2) is simplified using the Debye-Hückel linear approximation and substituted into Eq. (1), thereby reducing Eq. (1) to an analytically tractable linear equation.[30] The resulting Poisson-Boltzmann equation, together with the boundary conditions, reads as follows:

$$\frac{d^2\psi^*}{dy^{*2}} = \kappa^2 \psi^*,\ \kappa = \sqrt{\frac{2n_\infty z_v^2 e_0^2}{\varepsilon_0 \varepsilon_r k_B T}}, \tag{3}$$

$$\psi^*\Big|_{y^*=H^*} = \psi_\gamma^*,\ \frac{d\psi^*}{dy^*}\bigg|_{y^*=0} = 0, \tag{4}$$

where ψ_γ^* denotes the effective zeta potential and κ is the Debye-Hückel parameter. In contrast to the traditional Navier-slip model, we incorporate a slip-dependent zeta potential here to explain the modulation of the EDL by boundary slip, so that the zeta potential varies with the slip length. The effective zeta potential is expressed as a function of the slip length γ^* as follows[32,45]:

$$\psi_\gamma^* = \psi_0^* \left\{1 + \gamma^* \kappa \frac{\sinh(e_0 z_v \psi_0^*/k_B T)}{e_0 z_v \psi_0^*/k_B T}\right\}, \tag{5}$$

where ψ_0^* is the zeta potential with no-slip effect. By substituting the boundary constraints from Eq. (4) into Eq. (3), an analytical solution for the electrical potential can be obtained:

$$\psi^* = \psi_\gamma^* \frac{\cosh(\kappa y^*)}{\cosh(\kappa H^*)}. \tag{6}$$

Finally, the net charge density can be expressed as:

$$\rho_e^* = -\kappa^2 \psi_\gamma^* \frac{\cosh(\kappa y^*)}{\cosh(\kappa H^*)}. \tag{7}$$

2.2.Velocity and pressure distributions

The fluid is assumed to be incompressible, with a viscosity that depends on pressure. We consider a steady state, two-dimensional flow. The continuity and momentum equations are given by:[55]

$$\nabla^* \cdot \vec{u}^* = 0, \tag{8}$$

$$\rho^* \left(\vec{u}^* \cdot \nabla^* \vec{u}^*\right) = -\nabla^* p^* + \nabla \cdot \tau^* + \rho_e^* \vec{E}_s, \tag{9}$$

where, $\vec{u}^* = \left(u_x^*, u_y^*\right)$ denotes the fluid velocity vector, $u_x{}^*$ and $u_y{}^*$ represent the axial (x^*-direction) and vertical (y^*-direction) velocity components, respectively. In addition, ρ^* corresponds to the fluid density, p^* represents the pressure and $E_s{}^*$ is the induced streaming potential. τ^* is associated with the stress tensor, given by:[54,55]

$$\tau^* = \eta^* \left(\nabla \vec{u} \quad \vec{u}\right), \tag{10}$$

where η^* is fluid viscosity. In this study, considering fluid flow under high-pressure conditions, we adopt the exponential relationship proposed by Barus to better describe fluid viscosity, which is expressed as:[54-56]

$$\eta^* = \eta_0^* e^{\varepsilon^*\left(p^* - p_{ref}^*\right)}, \tag{11}$$

where $p_{ref}{}^*$ denotes the reference pressure. $\eta_0{}^*$ is the shear viscosity at the reference pressure $p^*=p_{ref}{}^*$ and ε^* is the pressure-viscosity coefficient. By expanding Eq. (8) and subsequently substituting Eq. (10) into Eq. (9), the continuity equation and the momentum equations in the x^* and y^* directions are obtained as follows:

$$\frac{\partial u_x^*}{\partial x^*} + \frac{\partial u_y^*}{\partial y^*} = 0, \tag{12}$$

$$\rho^*\left(u_x^* \frac{\partial u_x^*}{\partial x^*} + u_y^* \frac{\partial u_x^*}{\partial y^*}\right) = -\frac{\partial p^*}{\partial x^*} + 2\frac{\partial}{\partial x^*}\left(\eta^* \frac{\partial u_x^*}{\partial x^*}\right) + \frac{\partial}{\partial y^*}\left(\eta^* \frac{\partial u_y^*}{\partial x^*} + \eta^* \frac{\partial u_x^*}{\partial y^*}\right) + \rho_e^* E_s^*, \tag{13}$$

$$\rho^*\left(u_x^* \frac{\partial u_y^*}{\partial x^*} + u_y^* \frac{\partial u_y^*}{\partial y^*}\right) = -\frac{\partial p^*}{\partial y^*} + 2\frac{\partial}{\partial x^*}\left(\eta^* \frac{\partial u_y^*}{\partial x^*} + \eta^* \frac{\partial u_x^*}{\partial y^*}\right) + 2\frac{\partial}{\partial y^*}\left(\eta^* \frac{\partial u_y^*}{\partial y^*}\right). \tag{14}$$

With the pressure-dependent viscosity effect taken into account, the velocity, pressure, and viscosity all become unknown functions of both x^* and y^*. Therefore, pressure and flow velocity must be solved simultaneously. To facilitate the solution, we specify appropriate boundary conditions. Specifically, the axial velocity $u_x{}^*$ satisfies the slip boundary conditions and vertical velocity $u_y{}^*$ obeys no-penetration condition. At the channel centerline, symmetry conditions are imposed. Additionally, for a fluid with pressure-dependent viscosity, solving for the pressure yields an arbitrary constant. Therefore, a point-pressure condition is specified at the channel outlet to eliminate this arbitrary constant. A fixed volumetric flow rate Q^* is prescribed.[54,55] The mathematical expressions for these boundary conditions can be written as:

$$\left.\frac{\partial u_x^*}{\partial y^*}\right|_{y^*=0}=0,\ u_y^*\big|_{y^*=0}=0,\ u_x^*\big|_{y^*=H^*}+\gamma^*\left.\frac{\partial u_x^*}{\partial y^*}\right|_{y^*=H^*}=0,$$

$$u_y^*\big|_{y^*=H^*}=0,\ p^*\left(L^*,H^*\right)=p_{ref}^*,\ \int_{-H^*}^{H^*}u_x^*dy^*=\frac{Q^*}{W^*},\tag{15}$$

where W^* is the width of channel. For convenience in the subsequent derivation, the following dimensionless quantities are defined:

$$u_x=\frac{u_x^*}{U^*},\ u_y=\frac{u_y^*}{U^*H^*/L^*},\ x=\frac{x^*}{L^*},\ y=\frac{y^*}{H^*},\ p=\frac{p^*-p_{ref}^*}{3\eta_0^*U^*L^*/H^{*2}},$$

$$E_s=\frac{E_s^*}{E_0},\ U=\frac{Q^*}{2W^*H^*},\ \varepsilon=\frac{3\varepsilon^*\eta_0^*U^*L^*}{H^{*2}},\ a=\frac{H^*}{L^*},\ K=\kappa H^*,\ \gamma=\frac{\gamma^*}{H^*},$$

$$\psi_\gamma=\frac{e_0z_v\psi_\gamma^*}{k_BT},\ \psi=\frac{e_0z_v\psi^*}{k_BT},\ \eta=\frac{\eta^*}{\eta_0^*},\ u_r=\frac{\varepsilon_0\varepsilon_rk_BTE_0}{e_0z_v\eta_0^*U^*},\tag{16}$$

where U^* represents the characteristic velocity and a denotes the geometric scale ratio for the channel. The dimensionless pressure-viscosity coefficient is given by ε. η represents the dimensionless fluid viscosity. u_x is the dimensionless velocity component in the axial direction, u_y is the dimensionless velocity component in the vertical direction, and u_r is obtained by dividing the electroosmotic velocity by the characteristic velocity. ψ_γ is the dimensionless slip-dependent zeta potential. E_s denotes the dimensionless streaming potential. K is the electrokinetic width, defined as the ratio of the channel half-height to the EDL thickness. By substituting the above parameters and dimensionless variables into Eqs. (12)-(15), the corresponding dimensionless viscosity, continuity equation, momentum equation and boundary conditions are detailed below:

$$\eta=e^{\varepsilon p},\tag{17}$$

$$\frac{\partial u_x}{\partial x}+\frac{\partial u_y}{\partial y}=0,\tag{18}$$

$$0=-3\frac{\partial p}{\partial x}+2a^2\frac{\partial}{\partial x}\left(\eta\frac{\partial u_x}{\partial x}\right)+a^2\frac{\partial}{\partial y}\left(\eta\frac{\partial u_y}{\partial x}\right)+\frac{\partial}{\partial y}\left(\eta\frac{\partial u_x}{\partial y}\right)-u_rE_sK^2\psi_\gamma,\tag{19}$$

$$0=-3\frac{\partial p}{\partial y}+a^4\frac{\partial}{\partial x}\left(\eta\frac{\partial u_y}{\partial x}\right)+a^2\frac{\partial}{\partial x}\left(\eta\frac{\partial u_x}{\partial y}\right)+2a^2\frac{\partial}{\partial y}\left(\eta\frac{\partial u_y}{\partial y}\right),\tag{20}$$

$$\left.\frac{\partial u_x}{\partial y}\right|_{y=0}=0,\ u_y\big|_{y=0}=0,\ u_y\big|_{y=1}=0,\ u_x\big|_{y=1}+\gamma\left.\frac{\partial u_x}{\partial y}\right|_{y=1}=0,\ p(1,)=\ (\int_0^1u_xdy=1.\tag{21}$$

In this study, the fluid viscosity varies with pressure. This means that the nonlinear Eqs. (18)-(20) must be solved simultaneously. To acquire analytical solutions for the velocity, pressure and viscosity,

we employ the perturbation method,[55] using the dimensionaless pressure-viscosity coefficient ε as the small parameter and expanding all relevant flow variables into regular perturbation series in terms of ε. The specific formulation of the perturbation method is presented as follows:

$$X = \sum_{i=0} \varepsilon^i x_i. \tag{22}$$

where $X=p$, η, u_x, u_y. It should be noted that the contributions of third and higher order to the velocity and pressure fields are negligible. Because the viscosity depends exponentially on the pressure, however, its expansion generates a non-negligible third-order term. The viscosity is therefore carried up to third order, while the velocity and pressure fields are retained up to second order in ε.[55] Substituting Eq. (22) into Eqs. (17)-(21) and collecting terms of the same order in ε. The solution procedure for the asymptotic expansions at each order is described as follows.

2.2.1. Zero-order solution

Since the zero-order solution can be regarded as unidirectional flow, we assume that $u_{y0}=0$. Then, the expressions for governing equations and boundary conditions are given as follows:

$$\frac{\partial u_{x0}}{\partial x} = 0, \tag{23}$$

$$0 = -3\frac{\partial p_0}{\partial x} + \frac{\partial^2 u_{x0}}{\partial y^2} - u_r E_s K^2 \psi_\gamma \frac{\cosh(Ky)}{\cosh(K)}, \tag{24}$$

$$0 = -3\frac{\partial p_0}{\partial y}, \tag{25}$$

$$\left.\frac{\partial u_{x0}}{\partial y}\right|_{y=0} = 0,\ u_{x0}\big|_{y=1} + \gamma \left.\frac{\partial u_{x0}}{\partial y}\right|_{y=1} = 0,\ p_0(1,1) = 0,\ \int_0^1 u_{x0} dy = 1. \tag{26}$$

.

The analytical solution for the zero-order equation is obtained as follows:

$$u_{x0} = \frac{A_0}{2}\left(1-y^2\right) + u_r E_s \psi_\gamma \left[\frac{\cosh(Ky)}{\cosh(K)} - 1\right] - \gamma\left(-A_0 + u_r E_s \psi_\gamma K \tanh(K)\right), \tag{27}$$

$$p_0 = \frac{1}{3} A_0 (1-x), \tag{28}$$

A_0 is expressed as:

$$A_0 = \frac{3\left(1 - u_r E_s \psi_\gamma \tanh K / K + \gamma u_r E_s \psi_\gamma K \tanh K + u_r E_s \psi_\gamma\right)}{1+3\gamma}. \tag{29}$$

To verify the correctness of the model, we neglect the streaming potential and set the slip length to zero in our results, so that the conditions become consistent with those in Housiadas' article.[55] The comparison shows that the distributions of the axial velocity u_{x0} and pressure p_0 obtained in this

study are in agreement with the expressions of Housiadas.[55]

2.2.2. First-order solution

Using the zero-order results, we simplify the first-order governing equations and corresponding boundary conditions as follows:

$$\eta_1 = p_0, \tag{30}$$

$$\frac{\partial u_{x1}}{\partial x} + \frac{\partial u_{y1}}{\partial y} = 0, \tag{31}$$

$$0 = -3\frac{\partial p_1}{\partial x} + 2a^2\frac{\partial^2 u_{x0}}{\partial x^2} + a^2\frac{\partial^2 u_{y1}}{\partial y \partial x} + \frac{\partial^2 u_{x1}}{\partial y^2} + \frac{\partial}{\partial y}\left(\eta_1\frac{\partial u_{x0}}{\partial y}\right), \tag{32}$$

$$0 = -3\frac{\partial p_1}{\partial y} + a^4\frac{\partial^2 u_{y1}}{\partial x^2} + a^2\frac{\partial^2 u_{x1}}{\partial x \partial y} + a^2\frac{\partial}{\partial x}\left(\eta_1\frac{\partial u_{x0}}{\partial y}\right) + 2a^2\frac{\partial^2 u_{y1}}{\partial y^2}, \tag{33}$$

$$\left.\frac{\partial u_{x1}}{\partial y}\right|_{y=0} = 0,\ u_{y1}\big|_{y=0} = 0,\ u_{y1}\big|_{y=1} = 0,\ u_{x1}\big|_{y=1} + \gamma\left.\frac{\partial u_{x1}}{\partial y}\right|_{y=1} = 0,$$

$$p_1(1,1) = 0,\ \int_0^1 u_{x1}dy = 0. \tag{34}$$

Using Eqs. (30)-(34), the analytical solutions for the first-order pressure components and velocity are obtained as follows:

$$u_{x1} = \frac{E_s\psi_\gamma(x-1)\operatorname{sech}K\left(\left(K-3Ky^2\right)\cosh(Ky) + 2K\cosh(Ky) + 3\left(y^2-1\right)\sinh KA_0u_r\right)}{6K}, \tag{35}$$

$$u_{y1} = \frac{E_s\psi_\gamma A_0u_r\left(-2\operatorname{sech}K\sinh(Ky) + y\left(K\left(y^2-1\right) - \left(y^2-3\right)\tanh K\right)\right)}{6K}, \tag{36}$$

$$p_1 = \frac{1}{90K^4}A_0\left(5K^4\left((x-1)^2 + a^2\left(y^2-1\right)\right)A_0 + 5E_sK^3\psi_\gamma\sinh K\left(K\left(-3(x-1)^2 + a\left(3y^2+1\right)\right)\right)\right.$$
$$\left.\cosh K - 4a^2K\cosh(Ky) + 3\left((x-1)^2 - a^2\left(y^2-1\right)\right)\sinh K\right)u_r\Big). \tag{37}$$

To verify the correctness of the solution, we compared the first-order analytical solution including the axial velocity u_{x1}, the vertical velocity u_{y1} and the pressure p_1 obtained in this study with the results of Housiadas.[55] The results show a high degree of agreement under the degenerate conditions, fully confirming the accuracy of the present model and the solution procedure.

2.2.3. Second-order solution

Applying the same treatment to the second-order equations yields simplified continuity and momentum equations, along with their boundary conditions, as follows:

$$\eta_2 = p_1 + \frac{1}{2}p_0^2, \tag{38}$$

$$\frac{\partial u_{x2}}{\partial x}+\frac{\partial u_{y2}}{\partial y}=0, \tag{39}$$

$$0=-3\frac{\partial p_2}{\partial x}+2a^2\frac{\partial}{\partial x}\left(\frac{\partial u_{x2}}{\partial x}+\eta_1\frac{\partial u_{x1}}{\partial x}\right)+a\frac{\partial}{\partial y}\left(\frac{1}{a}\frac{\partial u_{x2}}{\partial y}+a\frac{\partial u_{y2}}{\partial x}+\eta_1\frac{1}{a}\frac{\partial u_{x1}}{\partial y}+\eta_2\frac{1}{a}\frac{\partial u_{x0}}{\partial y}\right), \tag{40}$$

$$0=-3\frac{\partial p_2}{\partial y}+a^3\frac{\partial}{\partial x}\left(\frac{1}{a}\frac{\partial u_{x2}}{\partial y}+a\frac{\partial u_{y2}}{\partial x}+\eta_1\frac{1}{a}\frac{\partial u_{x1}}{\partial y}+\eta_2\frac{1}{a}\frac{\partial u_{x0}}{\partial y}\right)+2a^2\frac{\partial}{\partial y}\left(\frac{\partial u_{y2}}{\partial y}+\eta_1\frac{\partial u_{y1}}{\partial y}\right), \tag{41}$$

$$\left.\frac{\partial u_{x2}}{\partial y}\right|_{y=0}=0,\ u_{y2}\big|_{y=0}=0,\ u_{y2}\big|_{y=1}=0,\ u_{x2}\big|_{y=1}+\gamma\left.\frac{\partial u_{x2}}{\partial y}\right|_{y=1}=0,$$

$$p_2(1,1)=0,\ \int_0^1 u_{x2}dy=0. \tag{42}$$

From Eq. (38), we find that the second-order viscosity includes both the first-order pressure contribution and a squared zero-order pressure term. This differs fundamentally from the linear dependence of viscosity on pressure. In fact, using the linear formula[30,52] $\eta(p)=\eta_0(1+\varepsilon p)$ yields a second-order viscosity correction ($\eta_2=p_1$) that depends solely on the first-order pressure, with no dependence on the zero-order pressure. The second-order solution follows from a procedure analogous to that used for the first-order. Because the resulting expressions are excessively long, they are provided in the **Supporting Materials**.

2.3. Streaming potential

We have derived asymptotic solutions for the electrokinetic flow velocity and the fluid pressure. However, the streaming potential E_s remains to be determined. It can be obtained by applying the electroneutrality condition,[30] which requires that the net ionic current per unit width I^* be zero, as given by the following expression:

$$I^*=I_s^*+I_c^*=0, \tag{43}$$

where I_s^* is the streaming current and I_c^* is the conduction current.[30,43] Their expressions are given by:

$$I_s^*=\int_0^{L^*}\int_{-H^*}^{H^*}e_0z_v\left(n_+-n_-\right)u_x^*dy^*dx^*, \tag{44}$$

$$I_c^*=\int_0^{L^*}\int_{-H^*}^{H^*}e_0z_v\left(n_++n_-\right)\frac{e_0z_vE_s^*}{f}dy^*dx^*, \tag{45}$$

where f is the friction coefficient of ions and $n_\pm$denotes the ionic number concentration of both the cations and the anions. By the Debye-Hückel linearization approximation, the ionic number concentration is simplified as follows:[30]

$$n_\pm=n_\infty\exp\left[\mp\qquad\qquad\mp\right. \tag{46}$$

Substituting the dimensionless parameters, Eq. (43) can be simplified to:

$$\int_0^1\int_0^1 \psi u_x dydx = Mu_r E_s, \tag{47}$$

where $M=e^2{}_0z^2{}_v\eta^*{}_0/k_BTf\varepsilon_0\varepsilon_r$ is the dimensionless ion friction coefficient. Inserting the expressions for u_x and ψ into Eq. (47) shows that E_s obeys the following cubic equation, from which the dimensionless streaming potential is obtained as:[30]

$$T_0E_s^3 + T_1E_s^2 + T_2E_s + T_3 = 0. \tag{48}$$

From Eq. (48), the dimensionless streaming potential E_s is derived as:

$$E_s = \left(-\frac{n_1}{2} + \left(\frac{n_1^2}{4} + \frac{m_1^3}{27} \right)^{\frac{1}{2}} \right)^{\frac{1}{3}} + \left(-\frac{n_1}{2} - \left(\frac{n_1^2}{4} + \frac{m_1^3}{27} \right)^{\frac{1}{2}} \right)^{\frac{1}{3}} - \frac{T_2}{3T_0}, \tag{49}$$

The expressions for m_1 and m_2 are given below:

$$m_1 = \frac{3T_0T_2 - T_1^2}{3T_0^2},\ n_1 = \frac{27T_0^2T_3 - 9T_0T_1T_2 + 2T_1^3}{27T_0^3}. \tag{50}$$

The expressions for the coefficients T_0, T_1, T_2 and T_3 in Eq. (50) are provided in the **Supporting Material**.

2.4. Electrokinetic energy conversion efficiency

Electrokinetic flow provides a direct route from fluid mechanical energy to electrical energy, offering broad application prospects in energy harvesting. Specifically, when a pressure gradient drives fluid motion, a streaming current is generated. As this current performs work through an external load, mechanical energy is converted into electrical energy. Based on the previously derived distributions of the velocity field, the pressure field, and the electrical potential, the electrokinetic energy conversion efficiency can be further calculated. This efficiency is defined as the ratio of the output electrical power to the input power,[30-32] expressed as:

$$\xi = \frac{P_{out}^*}{P_{in}^*}, \tag{51}$$

where the output power $P_{out}{}^*$ is governed by the streaming current and streaming potential, whereas the input power $P_{in}{}^*$ is determined by the pressure gradient together with the volumetric flow rate.

$$P_{out}^* = \frac{\left|I_s^*E_s^*\right|}{4},\ P_{in}^* = \left| \left(-\frac{\partial p^*}{\partial x^*} \right)_m Q_{in}^* \right|, \tag{52}$$

where $\left(-\frac{\partial p^*}{\partial x^*} \right)_m$ is the average pressure gradient in the x^*-direction, disregarding the streaming potential $E_s{}^*$. Its expression is:

$$\left(-\frac{\partial p^*}{\partial x^*}\right)_m = \frac{1}{H^* L^*}\int_0^{L^*}\int_0^{H^*} -\frac{\partial p^*}{\partial x^*}\bigg|_{E_s^*=0} dx^* dy^*. \tag{53}$$

Where the expression for the dimensionless pressure p neglecting the streaming potential is:

$$p|_{E_s=0} = \frac{1}{30K(1+3\gamma)^3}\Big(30a^2\varepsilon^2 y^2 + K\big(-30(1+3\gamma)^2(x-1)+15\varepsilon(1+3\gamma)\big((x-1)^2+a^2$$
$$\left(y^2-1\right)\big)-2\varepsilon^2\left(5(x-1)^3+3a^2\left(2+x\left(5y^2\right)-2\right)\right)\big)\big)\Big), \tag{54}$$

where the expression for the input volumetric flow rate Q_{in}^* driven solely by pressure is:

$$Q_{in}^* = \int_{-H^*}^{H^*}\int_0^{L^*} u_x^*\big|_{E_s^*=0} dx^* dy^* = \int_{-H^*}^{H^*}\int_0^{L^*} u_p^* dx^* dy^*, \tag{55}$$

where u_p^* is the velocity of the purely pressure-driven flow, neglecting the streaming potential (E_s^*=0). The dimensionless velocity u_p can be expressed as:

$$u_p = \frac{1}{40(1+3\gamma)^3}\left(-60(1+3\gamma)^2\left(y^2+2\gamma-1\right)+a^2\varepsilon^2\left(5y^4-6y^2+1\right)\right). \tag{56}$$

Through derivation, the expression for the electrokinetic energy conversion efficiency is obtained as:

$$\xi = \frac{u_r^2 E_s^2 K^2 M}{12\int_0^1\int_0^1 -\frac{\partial p}{\partial x}\Big|_{E_s=0} dxdy \int_0^1\int_0^1 u_p dxdy}. \tag{57}$$

3. Verification of the asymptotic solutions

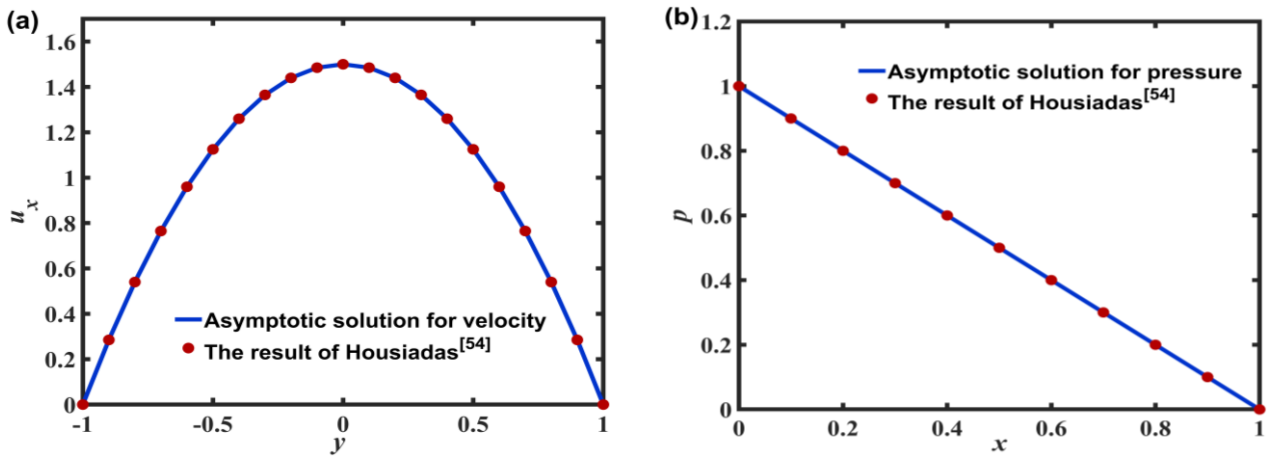


Fig. 2. Comparison of the present asymptotic solution with the exact solution obtained by Housiadas.[54] (a) Flow velocity (x = 1, ε = 0.1, a = 0.01, γ = 0). (b) Pressure (y = 1, ε = 0.1, a = 0.01, γ = 0).

In the previous section, we obtained second-order asymptotic analytical solutions for a fluid exhibiting pressure-dependent viscosity and slip-dependent zeta potential. To verify the applicability of the model, the asymptotic results for the velocity and pressure fields were benchmarked against the analytical solutions obtained by Housiadas.[54] He derived analytical expressions for Newtonian

fluids with pressure-dependent viscosity. Setting the streaming potential to zero, we recovered the model of Housiadas. With the same parameters, the velocity and pressure profiles are compared in Figs. 2(a) and 2(b), showing excellent agreement.

4. Results and Discussion

Table 1. Parameters for the working fluid employed in the channel.

Fluid characteristics	Value
Absolute temperature T	298K
Vacuum permittivity ε_0	8.85×10^{-12}F/m
Relative dielectric constant ε_r	732
Characteristic velocity U^*	1.667×10^{-7}m/s
Elementary charge e_0	1.60×10^{-19}C
Boltzmann constant k_B	1.38×10^{-23}J/K
Fluid density ρ^*	10^3kg/m^3
Fluid viscosity η_0^*	10^{-3}kg/(m·s)
Ionic valence z_v	1
Ion friction coefficient f	3.20×10^{-12}kg/s
Length of microchannels L^*	1μm~10μm
Height of microchannels H^*	10nm~100nm

In Section 2, we obtained asymptotic analytical solutions for the velocity and pressure fields of a fluid with pressure-dependent viscosity. The streaming potential and the energy conversion efficiency were then evaluated from these solutions. The principal physical parameters, along with the properties of the electrolyte solution, are summarized in Table 1. Moreover, the magnitude of the effective zeta potential is less than 25 mV. After normalization, the dimensionless effective zeta potential $|\psi_\gamma| \leq 1$. The zeta potential for the no-slip case is ψ_0=-0.6. In addition, the dimensionless electrokinetic width K falls within the range 1 to 15.The other key dimensionless parameters are set as u_r=1, a=0.00-0.01, and M=0.3. The nondimensional pressure-viscosity coefficient parameter ε is restricted to the range $0 \leq \varepsilon \leq 1$ in the present study. The effects of these parameters on the flow characteristics are analyzed in detail in the subsequent section.

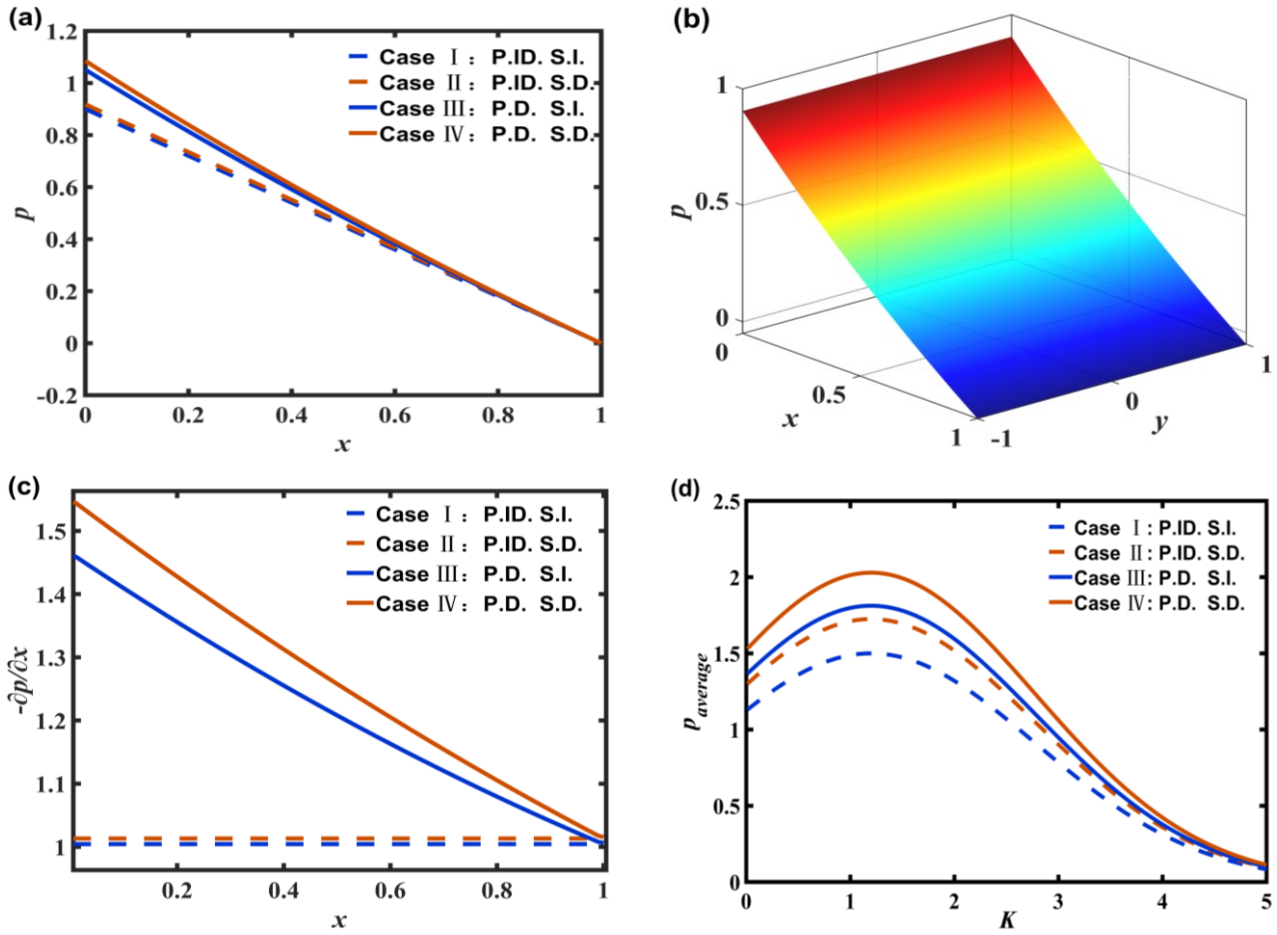


Fig. 3. Variations of pressure and pressure gradient with dimensionless axial distance x in slip-independent (S.I.) and slip-dependent (S.D.) zeta potential cases for pressure-independent (P.ID.) and pressure-dependent (P.D.) viscosities ($\gamma = 0.1$, $\varepsilon = 0.5$). (a)pressure ($y = 0$, $K = 5$). (b)The 3D plots of pressure ($K = 5$). (c)Pressure gradient ($y = 0$, $K = 5$). (d)Average pressure.

Fig. 3 compares the variations of pressure, pressure gradient and average pressure for S.D./S.I. zeta potentials and P.D./P.ID. viscosity models. As shown in Fig. 3(a), the pressure decreases monotonically from the inlet to the outlet of the channel, where the reference pressure is set to zero. The decline is not uniform: the profile is slightly concave, dropping more steeply near the inlet in the P.D. cases (Case III and Case IV), whereas it is nearly linear in the P.ID. cases (Case I and Case II). This difference reflects the spatial variation of the local viscosity. Because the Barus model makes the viscosity increase with pressure, the local resistance is largest where the pressure is highest, i.e., near the inlet, and the pressure must fall faster there. When the viscosity is held constant, the resistance is uniform along the channel and the pressure profile is nearly linear. In the pressure-independent viscosity cases (Case I and Case II), the pressure under the S.D. zeta potential condition exceeds that under the S.I. zeta potential condition(Case III and Case IV), the variation trend of pressure is similar. Mathematically, this phenomenon can be explained by the expressions for pressure, i.e., Eqs. (28) and (29). Accounting for the slip-dependent zeta potential effect elevates

the zeta potential and consequently boosts the pressure. A comparison of Case I with Case III and of Case II with Case IV shows that the pressure-dependent viscosity also raises the pressure. Fig. 3(b) clearly delineates the three-dimensional (3D) pressure distribution.

Fig. 3(c) shows the variation of the pressure gradient along the channel. For the P.ID. viscosity cases (Case I and Case II), the pressure gradient is independent of x. According to Eq. (17), setting the pressure-viscosity coefficient to zero, the fluid viscosity reduces to unity. In this circumstance, the pressure consists solely of the zero-order term, as described in Eqs. (28) and (29). Consequently, the partial derivative of pressure with respect to x is constant. For the P.D. cases (Case III and Case IV), the pressure gradient decreases monotonically from the inlet to the outlet. In addition, the pressure gradient in the S.D. condition exceeds that in the S.I. for both the P.D. and P.ID. viscosity models. Fig. 3(d) illustrates the variation of the average pressure with the dimensionless electrokinetic width K. It can be observed that the average pressure first increases and then decreases with K, reaching a peak at $K \approx 1.2$ across all four cases. The average pressure for the P.D. cases is higher than that for the P.ID. cases, and the S.D. conditions yield higher values than the S.I. conditions. Thus, both pressure-dependent viscosity and slip-dependent zeta potential increase the average pressure.

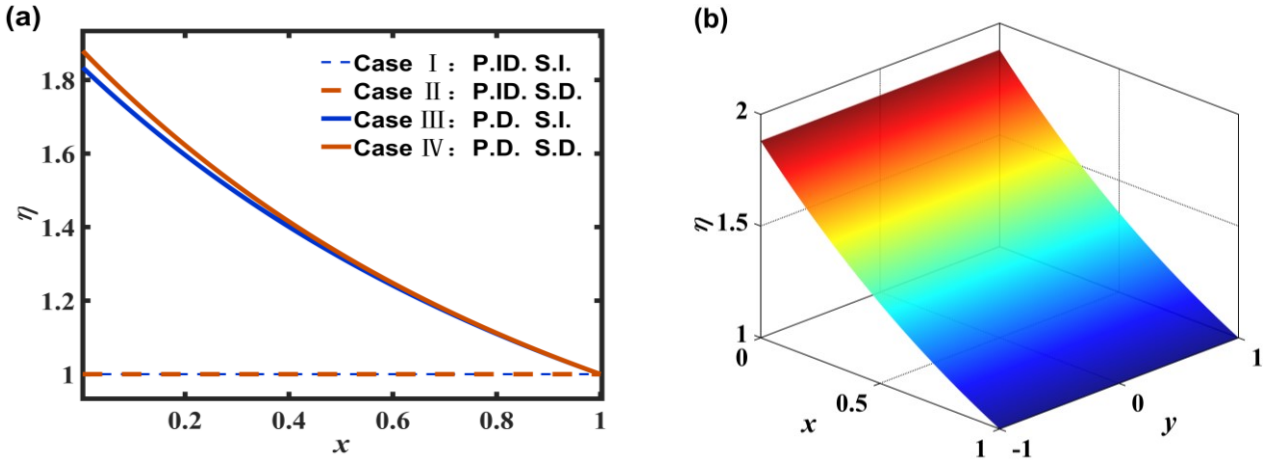


Fig. 4. Variation of fluid viscosity with the dimensionless axial distance x in slip-independent (S.I.) and slip-dependent (S.D.) zeta potential cases for pressure-independent (P.ID.) and pressure-dependent (P.D.) viscosities ($\gamma = 0.1$, $K = 5$, $\varepsilon = 0.5$). (a)Fluid viscosity ($y = 0$). (b)The 3D plots of fluid viscosity.

Fig. 4(a) illustrates the change in fluid viscosity in the S.D. zeta potential and pressure-dependent viscosity cases. For the P.ID. viscosity cases (Case I and Case II), the dimensionless fluid viscosity remains at unity throughout the channel, since the pressure-viscosity coefficient is zero in Eq. (17). For the P.D. cases (Case III and Case IV), the fluid viscosity gradually decreases from the channel inlet to the outlet, following the pressure distribution. Because the Barus model makes the viscosity vary exponentially with pressure and the pressure is highest at the inlet,

the viscosity is also highest there and it approaches unity as the pressure falls to zero at the outlet. Fig. 4(a) may therefore be regarded as the exponential image of the pressure profile in Fig. 3(a). Thus, the pressure-dependent viscosity effect can change the distribution of fluid viscosity. Moreover, we can find that the slip-dependent zeta potential can lead to an increase in fluid viscosity, as seen from the small offset between the S.D. and S.I. curves. This is because fluid viscosity varies exponentially with pressure. The slip-dependent zeta potential induces a rise in pressure, which in turn increases fluid viscosity. Fig. 4(b) presents a three-dimensional (3D) schematic of fluid viscosity as a function of the coordinates x and y. The viscosity is essentially invariant in the transverse direction and varies only with the axial coordinate, confirming that the pressure and viscosity are governed predominantly by the axial flow.

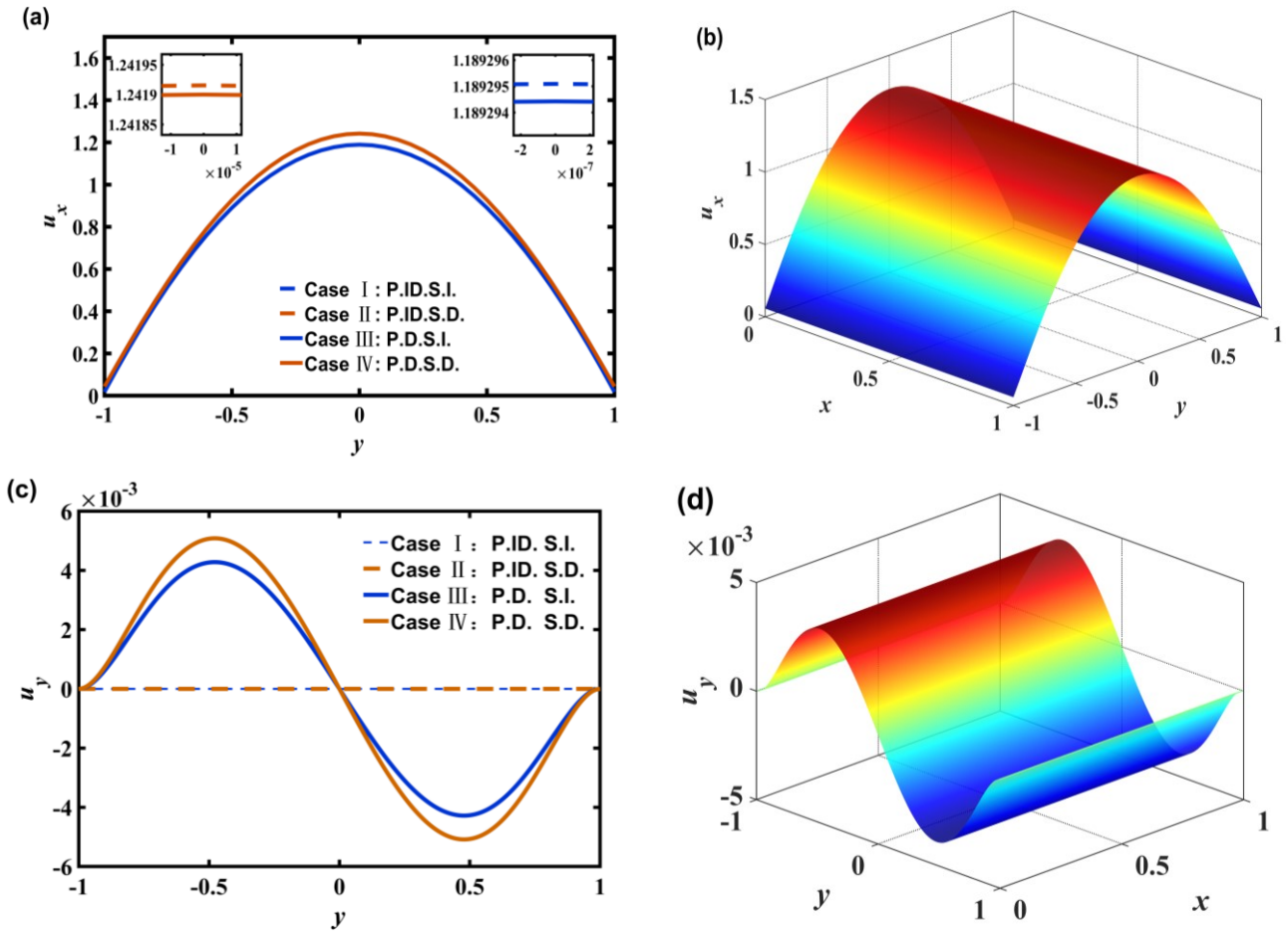


Fig. 5. Variations of the velocity with vertical distance y in slip-independent (S.I.) and slip-dependent (S.D.) zeta potential cases for pressure-independent (P.ID.) and pressure-dependent (P.D.) viscosities ($\gamma = 0.1$, $\varepsilon = 0.5$). (a)Axial velocity ($x = 1$, $K = 5$). (b)The 3D plots of axial velocity ($K = 5$). (c)Vertical velocity ($x = 1$, $K = 5$). (d)The 3D plots of vertical velocity ($K = 5$).

Fig. 5(a) describes the axial velocity distribution in the S.I. and S.D. zeta potential cases for the P.ID. and P.D. viscosity models. The axial velocity exhibits a parabolic profile, reaching its

maximum at the center and its minimum at the wall. In the P.D. viscosity cases (Case III and Case IV), a slip-dependent zeta potential enhances the flow velocity. This enhancement arises from the competition between elevated pressure and increased viscosity. The slip-dependent zeta potential effect boosts the pressure while simultaneously raising the fluid viscosity. Nevertheless, the enhancement effect of pressure dominates over the viscosity increment, ultimately resulting in an increased flow velocity. In addition, axial velocity increases more rapidly at the center of channel, while it increases more slowly near the wall. By comparing Case I with Case III and Case II with Case IV, it can be found that the P.D. viscosity slightly reduces the velocity. This can be attributed to the pressure-dependent viscosity effect, which simultaneously elevates pressure and viscosity. Since the viscosity increment plays a dominant role, the flow velocity is reduced. Fig. 5(b) shows the three-dimensional surface distribution of the axial velocity as a function of the coordinates x and y. The velocity forms a ridge-like surface. At any axial position, the axial velocity attains its maximum at the channel centerline and decreases monotonically toward the walls, which is the same as in Fig. 5(a). The streamwise decay of the crest is consistent with the monotonic decrease of the pressure and of the driving pressure gradient along the channel shown in Figs. 3(a) and 3(c).

Fig. 5(c) shows the variation of the vertical velocity. For the P.ID. viscosity cases (Case I and Case II), the vertical velocity is zero. The reason is that setting the pressure-viscosity coefficient to zero reduces the two-dimensional problem to a one-dimensional one. For the P.D. cases (Case III and Case IV), the vertical velocity exhibits a centrally symmetric wave-like profile. From Eq. (36), the vertical velocity proves to vary cubically with y. Moreover, the vertical velocity vanishes at both walls owing to the no-penetration boundary condition in Eq. (15). Furthermore, a marked predominance of the axial velocity over the vertical velocity is visible in Fig. 5(a). In addition, the vertical velocity in the S.D. condition is greater than that in the S.I. condition, because the slip-dependent zeta potential raises the effective zeta potential and thereby strengthens the electrokinetic driving that generates the secondary flow. This phenomenon indicates that the slip-dependent zeta potential effect not only enhances the vertical velocity but also increases the axial velocity. Fig. 5(d) illustrates the three-dimensional distribution of the vertical velocity as a function of x and y. The surface exhibits central symmetry in y and varies only weakly along x.

Fig. 6(a) illustrates the variation of the streaming potential with the dimensionless electrokinetic width K in the pressure-dependent and pressure-independent viscosity cases, accounting for two slip conditions: the S.I. and the S.D. zeta potential. It can be observed that the streaming potential decreases with increasing K for a given pressure-viscosity coefficient and slip length. This occurs because a larger K corresponds to a thinner electrical double layer, which reduces the number of freely mobile ions and thereby reduces both the streaming current and the streaming potential. A

comparison of Cases III and IV reveals that the streaming potential in the S.D. zeta potential condition is greater than that in the S.I. zeta potential condition. This indicates that the slip-dependent zeta potential can enhance the streaming potential. When the slip-dependent zeta potential effect is considered, the flow velocity increases. This enhances the convective transport of ions within the EDL, thereby elevating the streaming potential. In the slip-independent zeta potential cases (Case I and Case III), the pressure-dependent viscosity slightly reduces the streaming potential, since the associated reduction in flow velocity decreases the number of ions carried by the flow. Fig. 6(b) illustrates the variation of the streaming potential with both the electrokinetic width and the pressure dependence coefficient of viscosity. The streaming potential decreases with increasing pressure-viscosity coefficient. To elucidate the effects of slip length and pressure-viscosity coefficient on the streaming potential, 3D surface plots are presented in Fig. 6(c). The streaming potential increases with increasing slip length.

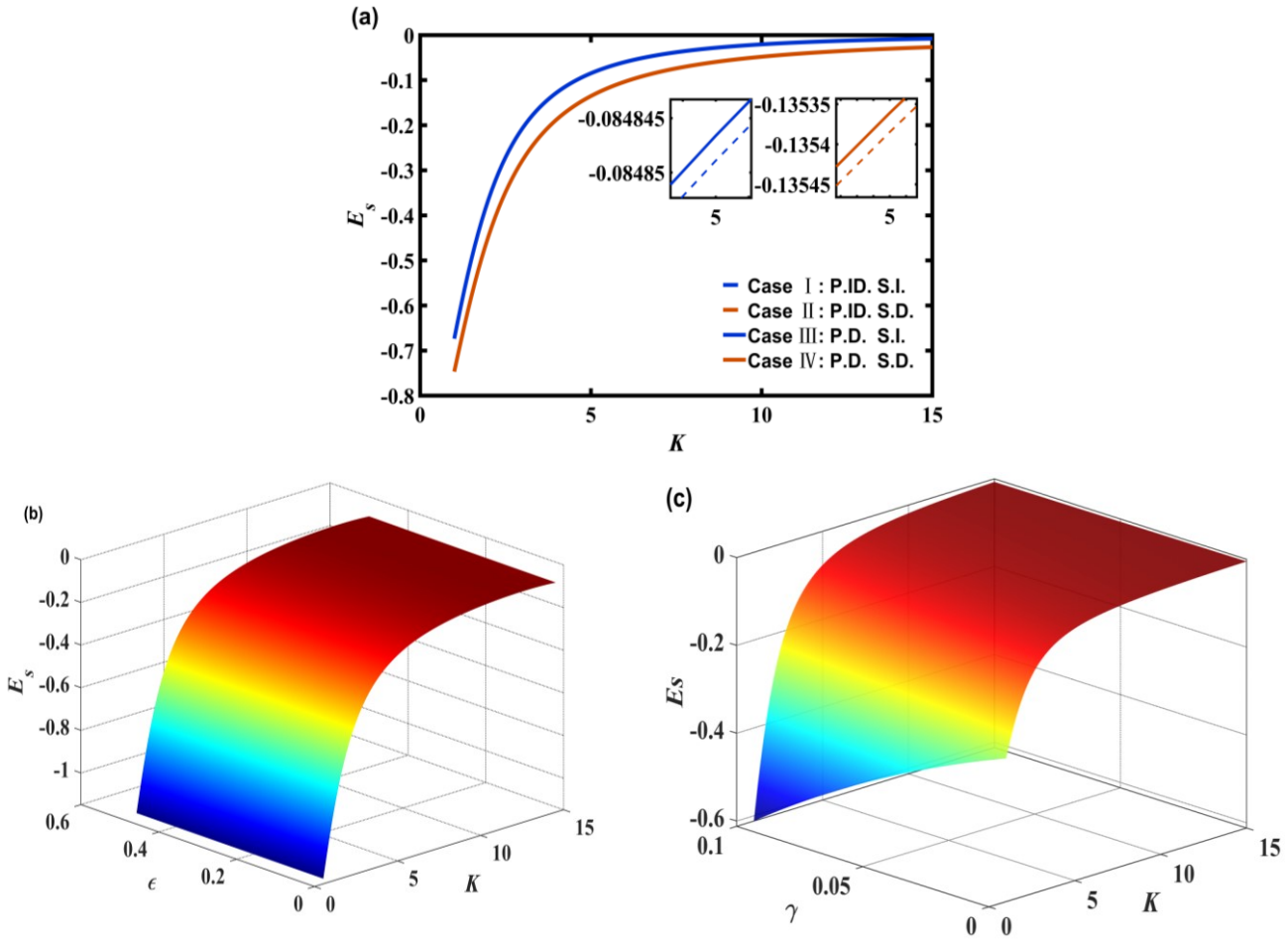


Fig. 6. (a)Variation of the streaming potential with the dimensionless electrokinetic width K in slip-independent (S.I.) and slip-dependent (S.D.) zeta potential cases for pressure-independent (P.ID.) viscosity and pressure-dependent (P.D.) viscosity ($\gamma = 0.1$, $\varepsilon = 0.5$). (b)The 3D plots of E_s via K and ε ($\gamma = 0.1$). (c)The 3D plots of E_s via K and γ ($\varepsilon = 0.5$).

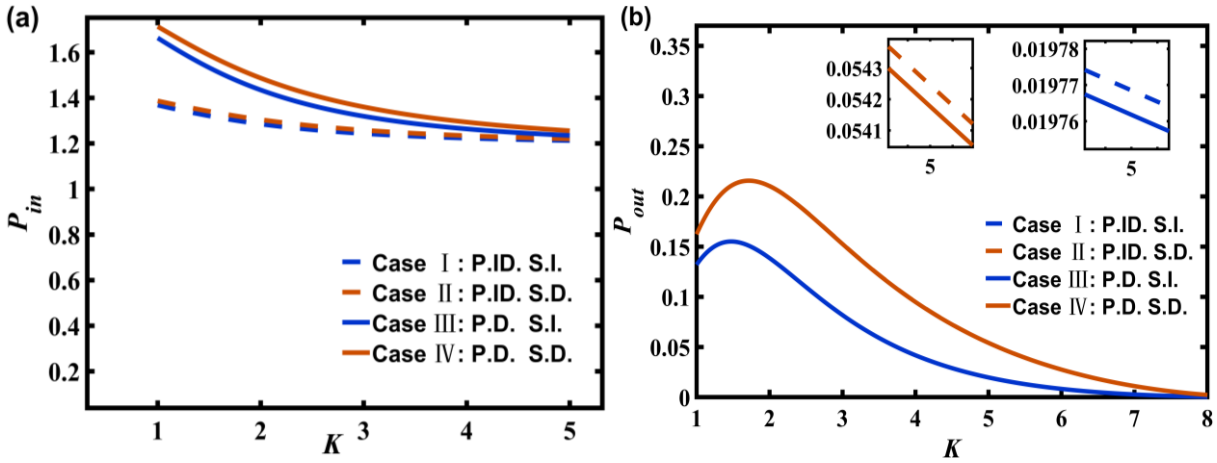


Fig. 7. Variations of input power and output power with the dimensionless electrokinetic width K in slip-independent (S.I.) and slip-dependent (S.D.) zeta potential cases for pressure-independent (P.ID.) and pressure-dependent (P.D.) viscosities. (a)Input power (γ =0.1, ε = 0.5). (b)Output power (γ = 0.1, ε = 0.5).

To gain a deeper understanding of the influence exerted by the pressure-dependent viscosity and slip-dependent zeta potential on the electrokinetic flow, we further investigate the variation of the input power, the output power, and the electrokinetic energy conversion efficiency. Fig. 7(a) describes the variation of the input power with the dimensionless electrokinetic width K. It shows that the S.D. zeta potential can cause an increase in input power in the P.D. viscosity cases (Case III and Case IV) and the P.ID. viscosity cases (Case I and Case II). The primary reason is that the slip-dependent zeta potential enhances both the flow velocity and the pressure gradient. Consequently, according to Eqs. (52)—(55), the input power also increases. The pressure-dependent viscosity effect can significantly increase the input power, as demonstrated by comparing Case I with Case III and Case II with Case IV. It elevates the pressure gradient (Fig. 3(c)) while reducing the flow velocity (Fig. 5(a)). However, since the extent of the pressure gradient increase is larger than that of the velocity decrease, input power ultimately rises. Fig. 7(b) illustrates the variation of output power. The P.D. effect leads to a slight reduction in output power, which can be observed only in an enlarged diagram. Under the P.D. viscosity condition, a rise in pressure is associated with an increase in the fluid viscosity. This leads to a reduction in the axial velocity, thereby lowering the streaming potential and ultimately causing a decline in the output power. However, the slip-dependent zeta potential effect can significantly enhance the output power, because the S.D. zeta potential can enhance the flow velocity, resulting in a higher streaming current and hence a larger output power.

Fig. 8(a) illustrates the variation of the electrokinetic energy conversion efficiency with the dimensionless electrokinetic width K. The efficiency initially increases to a maximum value, and then gradually declines as K increases. The P.D. viscosity effect can decrease the conversion efficiency. The reason is that the P.D. viscosity effect increases the input power and reduces the

output power. However, the slip-dependent zeta potential can enhance the conversion efficiency. This improvement occurs because the S.D. zeta potential significantly enhances both the output and the input power. Crucially, the magnitude of an increase in the output power far exceeds that of the input power, thereby raising the energy conversion efficiency. Thus, Case II exhibits a higher energy conversion efficiency than all other cases (I, III, and IV). In the P.ID. viscosity cases (Case I and Case II), the maximum electrokinetic energy conversion efficiencies for the S.D. and S.I. are 12.2% and 8.4%, respectively, representing an enhancement of 45.24%. By contrast, in the P.D. viscosity cases (Case III and Case IV), the maximum efficiencies are 10.9% and 7.5%, respectively, which represent an enhancement of 45.33%. Fig. 8(b) shows the variation of efficiency with the pressure-viscosity coefficient and K. As expected, the energy conversion efficiency decreases with increasing pressure-viscosity coefficient. Fig. 8(c) presents a 3D plot of the efficiency as a function of the slip length and K, revealing an upward trend with increasing slip length.

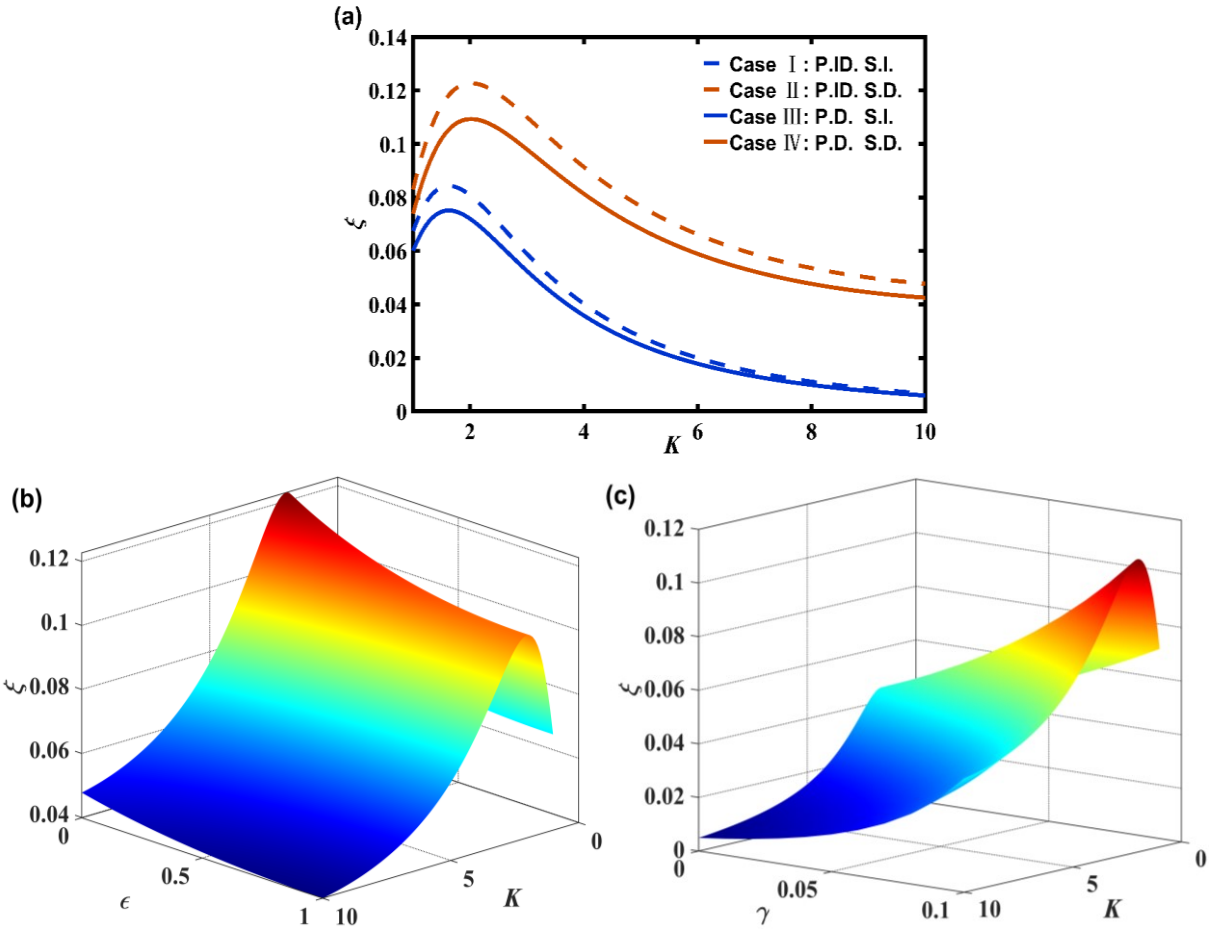


Fig. 8. (a)Variations of electrokinetic energy conversion efficiency with the dimensionless electrokinetic width K in slip-independent (S.I.) and slip-dependent (S.D.) zeta potential cases for pressure-independent (P.ID.) and pressure-dependent (P.D.) viscosities. ($\gamma = 0.1$, $\varepsilon = 0.5$). (b)Three-dimensional plots of the EECE as a function of K and ε ($\gamma = 0.1$). (c)Three-dimensional plots of the EECE as a function of K and γ ($\varepsilon = 0.5$).

5. Conclusion

This study addresses the electrokinetic flow and energy conversion of fluids exhibiting both pressure-dependent viscosity and slip-dependent zeta potential. The governing equations for two-dimensional flow are solved using the perturbation method, yielding analytical solutions for velocity, pressure and streaming potential, from which the energy conversion efficiency is then evaluated. The main findings are summarized as follows:

Under the slip-dependent zeta potential effect, the streaming potential, axial velocity, vertical velocity, fluid viscosity, pressure, output power, and input power are all increased. As a result, electrokinetic energy conversion efficiency is improved by this effect.

The pressure-dependent viscosity effect results in increased pressure and viscosity, as well as decreased axial velocity and streaming potential, and the appearance of a vertical velocity. It can reduce the output power while increasing the input power, leading to a reduction in electrokinetic energy conversion efficiency.

By comparing the four cases, it is found that the energy conversion efficiency of Case II is higher than those of Case I, Case III and Case IV, with a maximum efficiency of 12.2%. In the P.D. viscosity cases (Case III and Case IV), the maximum electrokinetic energy conversion efficiencies for the S.D. and S.I. zeta potentials are 10.9% and 7.5%, respectively, representing an enhancement of 45.33%.

Acknowledgements

This work was supported by Natural Science Foundation of Inner Mongolia (Approval Nos.2025LHMS01010, 2025ZD024, 2024QN01001).

Declaration of competing interest

The author declares that there is no actual or potential conflict of interest including any financial, personal or other relationships with other people.

References

[1]Li H, Du Y and Ma X 2025 J. Chem. Phys. 163 011001

[2]Liu Q, Yu Y F, Zhao W S and Li H 2020 Chin. Phys. B 29 010701

[3]Wang D, Li X N, Zhou J Y, Liu L Y and Chen G 2025 Chin. Phys. B 34 124702

[4]Shi H, Nie K, Dong B, Long M, Xu H and Liu Z 2019 Chem. Eng. J. 361 635-650

[5]Zhao J, Xu T and Yang B 2021 Vac. Cryog. 27 296-302 (in Chinese)

[6]Kim M, Wang B H, Jeong J, Min N K and Kwon K H 2012 J. Nanosci. Nanotechnol. 12 1530-1536

[7]Han J, Kang U and Moon E Y 2022 BioChip J. 16 255-269

[8]Yin M, Kim Z A and Xu B 2022 Adv. NanoBiomed Res. 2 2100117

[9]Dolatshahi R, Khatibi M and Ashrafizadeh S N 2026 Langmuir 42 0743-7463
[10]Xu D, Yan M and Xie Y 2024 Electrophoresis 45 244-265
[11]Ruiz-Diaz J A, Mendez F, Ramos E A et al 2026 J. Thermophys. Heat Transf. 1-10
[12]Tracy J B and Crawford T M 2013 MRS Bull. 38 915-920
[13]Wu W 2018 Analyst 143 4819–4835
[14]Yuan S, Zhou M and Liu X 2023 Int. J. Heat Mass Transf. 206 123925
[15]Sun Y, Jiang R and Hu L 2023 Electrophoresis 44 1756-1773
[16]Liu Q S, Jian Y J and Yang L G 2011 J. Non-Newton. Fluid Mech. 166 478-486
[17]Vasista K N, Mehta S K and Pati S 2022 Chem. Eng. Process. 176 108940
[18]Xie Z Y, Jian Y J and Tan W C 2018 Sens. Actuators B Chem. 273 1257-1268
[19]Qian F, Yan H and Jiao K 2023 Colloids Surf. A 675 132002
[20]Sasmal C, Waghmare T and Chauhan A 2026 Soft Matter 22 589–603
[21]Jing D and Bhushan B 2013 Langmuir 29 6953–6963
[22]Qiao Y, Cui J, Xie Z and Chen X 2026 Electrochim. Acta 573 149143
[23]Fan X and Liu Y 2026 Phys. Fluids 38 052005
[24]Malekidelarestaqi M, Mansouri A and Chini S F 2018 Chem. Phys. Lett. 703 72-79
[25]Chanda S, Sinha S and Das S 2014 Soft Matter 10 7558-7568
[26]Mei L J, Yeh L H and Qian S Z 2017 Nano Energy 32 374-381
[27]Dhakar J and Bharti R P 2023 Int. Conf. Comput. Heat Mass Transf. (Cham: Springer Nature Switzerland) pp. 244-254
[28]Li C, Liu Z and Qiao N 2022 Electrochim. Acta 419 140421
[29]Li C, Zhang Z and Li Z 2023 Electrochim. Acta 454 142379
[30]Jian Y J 2022 Int. J. Eng. Sci. 170 103590
[31]Chen X Y, Xie Z Y and Jian Y J 2024 Phys. Fluids 36 032025
[32]Liu Y, Wu Z and Liu G 2024 Phys. Scr. 99 025205
[33]Morikawa K, Chang C C and Kazoe Y 2025 Colloids Surf. A 719 137036
[34]Liu Y and Jian Y J 2025 Int. J. Eng. Sci. 213 104263
[35]Zhang Y, Zhao G and Zhang J 2025 J. Mol. Liq. 424 128263
[36]Liu Y, Jian Y and Yang C 2020 Energy 198 117401
[37]Liu Y B, Jian Y J and Yang C H 2020 Colloids Surf. A 591 124558
[38]Bansal A K, Suman S and Kumar M 2024 Eng. Appl. Artif. Intell. 133 108371
[39]Liu Y B. 2024 Chin. Phys. B 33 074101
[40]Zhang P, Liu Z, Liu X and Liu G 2025 Desalination 616 119402
[41]Ren Y and Stein D 2008 Nanotechnology 19 195707
[42]Yan Y, Sheng Q, Wang C, Xue J and Chang H C 2013 J. Phys. Chem. C 117 8050–8061

[43]Buren M, Jian Y J, Zhao Y C, Chang L and Liu Q S 2019 Beilstein J. Nanotechnol. 10 1628–1635
[44]Jing D and Bhushan B 2015 J. Colloid Interface Sci. 454 152-179
[45]Churaev N V, Ralston J, Sergeeva I P and Sobolev V D 2002 Adv. Colloid Interface Sci. 96 265–278
[46]Yang J and Kwok D Y 2002 J. Phys. Chem. B 106 12851-12855
[47]Tretheway D C and Meinhart C D 2002 Phys. Fluids 14 L9-L12
[48]Tandon V and Kirby B. J. 2008 Electrophoresis 29 1102-1114
[49]Liu Z, Feng Y, Wang L, Liu Q and Liu G 2023 Int. J. Heat Mass Transf. 204 123874
[50]Guo X, Chen M and Li Y 2020 Trends Food Sci. Technol. 100 223-234
[51]Lei Z U, Xia X Z and Jia X L 2022 Chin. J. Aeronaut. 35 438-449
[52]Hron J, Malek J and Rajagopal K R 2001 R. Soc. Lond. Ser. A 457 1603–1622
[53]Rajagopal K R, Saccomandi G and Vergori L 2013 J. Math. Anal. Appl. 404 362-372
[54]Housiadas K D 2015 J. Rheol. 59 769–791
[55]Housiadas K D 2015 J. Non-Newton. Fluid Mech. 223 147-156
[56]Herbst R S, Harley C and Rajagopal K R 2025 Fluids 10 33
[57]Cui H H, Silber-Li Z H and Zhu S N 2004 Phys. Fluids 16 1803-1810
[58]Silber-Li Z, Cui H and Tan Y 2006 Acta Mech. Sin. 22 17-21